# Levelized cost of electricity evaluation of liquid sodium receiver designs through a thermal performance, mechanical reliability, and pressure drop analysis

Tim Conroy[a,*], Maurice N. Collins[a], James Fisher[b], Ronan Grimes[a]

[a]*Stokes Laboratories, Bernal Institute, School of Engineering, University of Limerick, Ireland*
[b]*Vast Solar, Level 10, 17-19 Bridge St, Sydney, NSW, 2000, Australia*

**Abstract**

The receiver in a concentrated solar power (CSP) tower system accounts for a considerable proportion of plant capital costs, and its role in converting radiant solar energy into thermal energy affects the cost of generated electricity. It is imperative to utilize a receiver design that has a high thermal efficiency, excellent mechanical integrity, minimal pressure drop, and low cost in order to maximize the potential of the CSP system. In the present work, thermal, mechanical, and hydraulic models are presented for a liquid tubular billboard receiver in a representative CSP plant. A liquid sodium heat transfer fluid as well as a number of receiver configurations of heat transfer area, tube diameter, and tube material have been analysed. The thermal analysis determines tube surface temperatures for an incident heat flux, thereby allowing for the calculation of thermal losses and efficiency. The mechanical analysis is carried out to establish creep deformation and fatigue damage that the receiver may undergo through a life service. The hydraulic analysis is concerned with calculating the required pumping power for each configuration. Results show that thermal efficiency increases for a decreasing heat transfer area, however reducing receiver area comes at the penalty of increasing tube surface temperatures and thermal stresses. The selection of tube diameter is critical, with small diameters yielding the greatest thermal efficiency and mechanical life, however the increased pressure drop reduces the overall plant efficiency due to a necessary increase in pumping power. The optimum receiver configuration is established by finding an appropriate trade-off between thermal performance, service life, pressure drop, and material costs, by using the levelized cost of electricity (LCOE) as the objective function. The analysis highlights necessary trade-offs required to optimise the design of a solar receiver.

*Keywords:* Liquid sodium receiver, LCOE, Thermohydraulic analysis, Mechanical analysis

## 1. Introduction

The development of renewable energy technologies has accelerated in recent times due to concerns with the environment, energy security and depletion rates of traditional fossil fuels. Solar energy has the greatest potential of all renewable resources, with 885 *million TWh* falling on the earth's surface each year (IEA, 2014). In terms of electricity

*Corresponding author
*Email address:* timothy.conroy@ul.ie (Tim Conroy)

generation, Photovoltaic (PV) and Concentrated Solar Power (CSP) are the two main solar energy mechanisms in use today. PV currently leads CSP in terms of commercial deployment, largely due to technological improvements and significant cost reductions in recent years. Cost effective energy storage is a significant challenge with PV technology however (IEA, 2015), meaning that a commercial system may struggle to satisfactorily meet grid demands due to its 'must take' nature and intermittent supply. The means of power generation with CSP is not dissimilar to that of a traditional coal-fired plant. CSP uses point and line focus techniques to generate thermal energy in a heat transfer fluid (HTF), which is in turn used to generate electricity using a steam turbine. The conversion of concentrated solar energy into thermal energy means that CSP can generate dispatchable electricity for the grid, through thermal storage mechanisms. The ability to store thermal energy means CSP is more flexible to grid demands than most other renewable energy technologies, with dispatchability being a key value adding asset to the system (Kolb et al., 2011). CSP is considered as a realistic candidate to supply intermediate and base load power demands (Slocum et al., 2011), and is fast emerging as a feasible technology that can alleviate fossil fuel dependence in locations with a high solar resource, projected to contribute to approximately 11% of global electricity production by 2050 (IEA, 2014).

Power tower technology is expected to play a major role in the future of CSP (IRENA, 2012). Tower systems can operate at higher temperatures that result in greater thermal storage potential and higher efficiencies in the thermodynamic power cycle (Ho and Iverson, 2014). The heliostat field and receiver contribute to a significant proportion of a plant's capital costs (Pitz-Paal, 2005); therefore maximizing the efficiency of the receiver will extract maximum potential of the heliostat field, helping to increase overall productivity and lower the cost of electricity generated. Reducing both electricity costs and capital costs is a key aim for CSP research and development, as this affects the ability of CSP to compete with other electricity generating technologies on a commercial level (IRENA, 2012).

There are a number of ways to optimise the receiver design in order to maximise thermal performance and reliability. The selection of an appropriate receiver HTF is one of the most important considerations made at the design stage, as it influences plant costs, receiver performance, and thermal storage characteristics (Pacio and Wetzel, 2013). A variety of working fluids such as water/steam, molten salts, and liquid metals have been tested and operated in liquid tubular receivers since the 1980's (Falcone, 1986). Sodium is a promising working fluid that may facilitate cost reductions and performance improvements for future CSP projects (Coventry et al., 2015). It is advantageous in receiver applications due to its large thermal conductivity and broad operational temperature range in the liquid phase ($371\,K - 1156\,K$). The thermal conductivity of liquid sodium is nearly two orders of magnitude greater than that of molten salt, this yields heat transfer coefficients that are an order of magnitude greater (Pacio et al., 2014). Improved heat transfer performance using liquid sodium should result in reduced receiver temperatures, meaning greater thermal efficiency and reduced thermomechanical strains. In an investigation by Boerema et al. (2012), it was found that a receiver using a liquid sodium HTF can be 57% smaller in heat transfer area than an equivalent molten salt receiver, allowing for greater thermal efficiency and reduced material costs. Disadvantages associated with liquid sodium includes its low specific heat capacity, rendering the requirement for large volumes for direct thermal energy storage systems, and it has a volatile exothermic reaction with air and water (Pacio and Wetzel, 2013). Despite its extensive

**Nomenclature**

| | |
|---|---|
| $a_s$ | solar absorptivity |
| $A$ | area ($m^2$) |
| $A_n, a_n, B_n, b_n$ | Fourier coefficients |
| $Bi$ | Biot number |
| $C_p$ | specific heat capacity ($J/kgK$) |
| $D$ | diameter ($m$) |
| $E$ | Young's Modulus ($GPa$) |
| $f$ | friction factor |
| $F$ | Fourier expression |
| $F_{view}$ | view factor |
| $G_{0,n}$ | wall temperature functions |
| $h$ | heat transfer coefficient ($W/m^2K$) |
| $I_o$ | capital cost (\$) |
| $k$ | thermal conductivity ($W/mK$) |
| $L$ | length ($m$) |
| $\dot{m}$ | mass flow rate ($kg/s$) |
| $n/N$ | number |
| $n_d/N_d$ | actual/allowable fatigue cycles |
| $Nu$ | Nusselt number |
| $O\&M$ | operation & maintenance ($\$/kW_e$) |
| $\Delta P$ | pressure drop ($kPa$) |
| $P$ | pressure ($kPa$) |
| $Pr$ | Prandtl number |
| $Q$ | power ($MW$) |
| $Q''$ | heat flux ($MW/m^2$) |
| $r$ | radius ($m$) |
| $r_d$ | discount rate |
| $Re$ | Reynolds number |
| $\Delta t_d/t_d$ | actual/allowable time ($hour$) |
| $T$ | temperature ($K$) |
| $\dot{W}$ | pumping power ($kW$) |

*Greek symbols*

| | |
|---|---|
| $\alpha$ | thermal expansion coefficient ($K^{-1}$) |
| $\delta$ | Stefan-Boltzmann constant ($W/m^2K^4$) |
| $\varepsilon$ | emissivity |
| $\epsilon$ | strain |
| $\eta$ | efficiency |
| $\theta$ | circumferential position ($rad$) |
| $\mu$ | dynamic viscosity ($Pa \cdot s$) |
| $\nu$ | Poisson's ratio |
| $\rho$ | density ($kg/m^3$) |
| $\sigma/\tau$ | normal/shear stress ($MPa$) |

*Sub/superscript*

| | |
|---|---|
| $\infty$ | ambient conditions |
| $array$ | solar array |
| $avg$ | average |
| $base$ | baseline |
| $conv$ | convection |
| $e$ | electrical |
| $el$ | element |
| $error$ | convergence error |
| $f$ | fluid |
| $hr$ | hour |
| $i/in$ | inside/inlet |
| $j$ | iteration step |
| $l$ | losses |
| $mat$ | material |
| $net$ | net input |
| $o, out$ | outside/outlet |
| $opt$ | heliostat field |
| $p$ | fatigue cycle type |
| $plant$ | CSP plant |
| $pump$ | HTF pump |
| $pwr$ | power block |
| $q$ | creep loading condition |
| $r, \theta, z$ | radial, circumferential, axial |
| $rad$ | radiation |
| $rcv$ | receiver |
| $ref$ | reflection |
| $rep$ | replacement |
| $si/so$ | inner/outer surface |
| $th$ | thermal |
| $trans$ | piping & storage |
| $tube$ | receiver tube |
| $vM$ | von Mises |
| $yr$ | year |

*Abbreviations*

| | |
|---|---|
| $CAPEX$ | capital expenditure |
| $CSP$ | concentrated solar power |
| $DNI$ | direct normal irradiance |
| $HTF$ | heat transfer fluid |
| $LCOE$ | levelized cost of electricity |
| $PV$ | photovoltaic |

use in the nuclear industry, there is relatively little operational experience with liquid sodium HTF in CSP applications in comparison to that of water/steam and molten salt. The IEA-SSPS receiver tests conducted at Almeria, Spain in the 1980's highlighted the advantages of sodium, where tests were conducted up to high heat fluxes ($\sim 2.5\, MW/m^2$), and thermal efficiencies of $\sim 90\%$ were reported (Schiel and Geyer, 1988). A sodium leak lead to a large spray fire in 1986, effectively shutting down any R&D activity using sodium. At this point in time, the only CSP plant utilising liquid sodium is at Vast Solar's Jemalong Solar Station facility in NSW, Australia (Coventry et al., 2015), which forms the basis of this analysis. Properties of liquid sodium are given in Fink and Leibowitz (1995).

Another method of increasing receiver performance is by decreasing the overall receiver heat transfer area, as this reduces convective and radiative heat losses to the environment. However, large heat fluxes can lead to extreme surface temperatures and thermal stresses, thereby significantly diminishing the mechanical reliability of the receiver through creep deformation and thermal fatigue cycling (Liao et al., 2014). CSP technology is expected to compete with commercial PV modules with warranties of $\sim 25$ years, therefore the receiver should be designed with excellent reliability (Fork et al., 2012).

The material used to construct the receiver tubes is an important consideration at the design stage, as mechanical integrity is largely dependant on the material chosen (Lata et al., 2008). Many receivers constructed to date employ stainless steel tubes due to its mechanical strength, compatibility with various heat transfer media, and relatively low cost, however other high temperature alloys are being investigated for compatibility with higher-temperature thermodynamic cycles (Kolb, 2011). The choice of material will have an affect on the overall reliability of the receiver, however material costs will have a large effect on selection.

Another method that can be employed in receiver design is to utilise small diameter tubes with thin walls (Liao et al., 2014). This will result in a smaller temperature gradients on the tube as the heat transfer coefficient increases with a decrease in diameter, meaning greater thermal efficiency and assisting in reducing thermal stresses. Reducing tube diameter will however result in an increase in pressure drop across the receiver (Rodríguez-Sánchez et al., 2014), thereby increasing the necessary pumping power for the system.

It is evident that a CSP thermal receiver must be designed with consideration given towards a number of performance criteria, namely: thermal performance, mechanical reliability, pumping requirement, and cost. The current work presents thermal, mechanical reliability and pressure drop models for a low cost, single pass billboard receiver with a liquid sodium working fluid. Theoretical thermal, mechanical, and hydraulic models are presented in order to calculate steady state receiver thermal performance, creep-fatigue damage due to sustained high temperature operation under stress and cyclic thermal events, and pressure drop. The analysis is conducted in order to determine the optimum receiver geometry and tube material for a modular CSP plant. The models are used to investigate various receiver geometries for three candidate tube materials of 304 Stainless Steel (UNS S30400), 316 Stainless Steel (UNS S31600), and nickel-iron-chromium alloy Alloy 800H (UNS N08810). The optimum receiver design is highlighted by using the levelized cost of electricity (LCOE) as a figure of merit, as it combines applicable performance characteristics.

## 2. Receiver model

The billboard receiver design is located externally with an equator facing heliostat field. The HTF is pumped from the cold storage tank and enters the receiver through the inlet header, where it is then distributed amongst a bank of tubes. The HTF becomes irradiated by the incident heat flux on the billboard panel, and fluid mixing in the outlet header determines the overall temperature of the fluid leaving the receiver. The design investigated in the present study shuttles the HTF through the tubes in a single pass; therefore the mass flow rate depends on the fluid inlet temperature, desired outlet temperature, incident power from the heliostat field, and receiver geometry. The analysis is concerned with tube diameters ranging from $0.006\,m$ to $0.02\,m$, all with a wall thickness of $0.001\,m$, and receiver plane areas ranging from $1 \sim 4\,m^2$. A minimum area of $1\,m^2$ was chosen as it represents the approximate image size of the furthermost located heliostat in the representative CSP plant (subtended sun angle multiplied by the focal length). The tube geometries investigated were chosen as they conform to the EN ISO 1127 standard for heat exchanger tubes, meaning that they should be readily available for a manufacturing process. A square receiver area is convenient for the control of flux distribution from the heliostat field using various aiming strategies (Salomé et al., 2013), therefore the present study analyses a range of receiver areas approximating a square shape. The receiver area is increased incrementally adding tubes to the receiver, while simultaneously extending the tube length by the value of tube diameter. An illustration of the receiver design is shown in Figure 1.

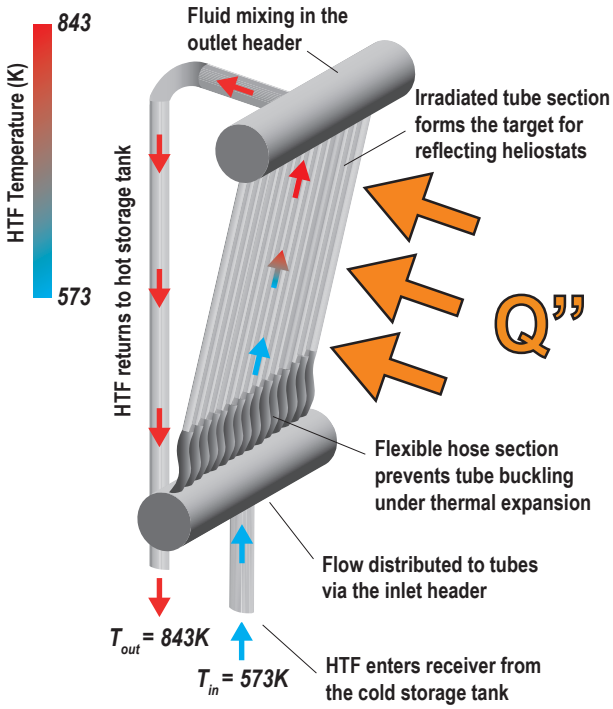


Figure 1: Liquid tubular billboard receiver

To determine tube material influences, three tube materials are modelled, namely: 304 Stainless Steel (UNS

S30400), 316 Stainless Steel (UNS S31600), and a nickel-iron-chromium alloy with Al and Ti additions, Alloy 800H (UNS N08810). The 304 and 316 stainless steels have a broad range of applications, and are relatively low cost in comparison to other high temperature candidate alloys such as Alloy 800H (Kolb, 2011). The Alloy 800H material is more expensive than the stainless steel alternatives, however it has excellent creep and fatigue strength at high temperatures. The materials selected are covered by the ASME Boiler & Pressure Vessel code (ASME, 2007), which stipulates guidelines in which to estimate the reliability of high temperature components in Section III: Subsection NH.

A maximum power input of $Q_{net} = 2\,MW$ is used, mimicking near design point conditions of the equator facing heliostat field that is the basis for the analysis. The reference field is constructed of 699 rectangular heliostats, each with $3.6\,m^2$ of reflective area, with automated azimuth-elevation tracking. This heliostat field is a simulated version of a field used at the Vast Solar CSP plant in Australia (Vast Solar, 2017). A uniform heat flux profile is applied for simplicity, which approximates the heat flux distribution yielded by an ideal heliostat aiming strategy, which aims to 'flatten' the heat flux distribution as best as possible.

The following subsections detail the mathematical models used in the analysis. The method for calculating tube surface temperatures is first described. These temperatures form the basis for calculating receiver thermal performance for the various heat loss modes and mechanical reliability. The theory behind calculating tube stresses that lead to creep and fatigue damage is then described, followed by the calculation procedure for hydraulic performance. Finally, the means in which LCOE is determined for each design is presented.

### *2.1. Thermal analysis*

The HTF enters the receiver heated section at 573 $K$ ($T_{in,\,z_{el}=1}$), and is assumed as being distributed to all tubes uniformly. At the various direct normal irradiance (DNI) conditions, the desired outlet temperature of 843 $K$ ($T_{out,\,z_{el}=N_{z_{el}}}$) is achieved by controlling the HTF mass flow rate, however an implementation of a minimum receiver volumetric flow rate of $3\,l/s$ (limited by the HTF pump) means that the desired outlet temperature may not be reached at lower DNI levels. A non-uniform heat flux distribution exists around the tube circumference due to curvature, influencing tube surface temperatures. A cosine distribution is used to approximate the exposure to the prescribed heat flux on the front of the tube $\left(\dot{Q}''_{so,\,z,\,\theta}\right)$, while adiabatic conditions are assumed for the insulation layer at the rear, described by Equation 1 and Figure 2.

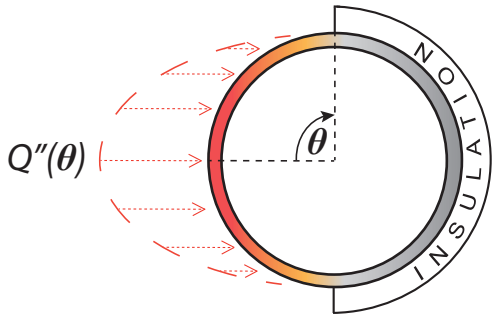


Figure 2: Cosine heat flux distribution on the tube

$$\dot{Q}''_{so,z,\theta} = \begin{cases} Q'' \cos(\theta) & 0 \le \theta \le \pi/2 \\ 0 & \pi/2 \le \theta \le 3\pi/2 \\ Q'' \cos(\theta) & 3\pi/2 \le \theta \le 2\pi \end{cases} \tag{1}$$

Modelling need only be carried out on a single receiver tube due to the assumption of a uniform heat flux across the billboard panel. Heat transfer calculations for the thermal model are initially performed on tube elements discretised in the axial direction ($z_{el}$), assuming steady, fully developed hydrodynamic and thermal boundary conditions. The circumferential temperature distribution around the tube is calculated by subdividing each axial element into circumferential elements ($\theta_{el}$). The thermal model performs heat transfer calculations on each axial element of the tube in an iterative manner until an energy balance is reached between heat transferred to the fluid and heat lost to the environment, shown in Figure 3.

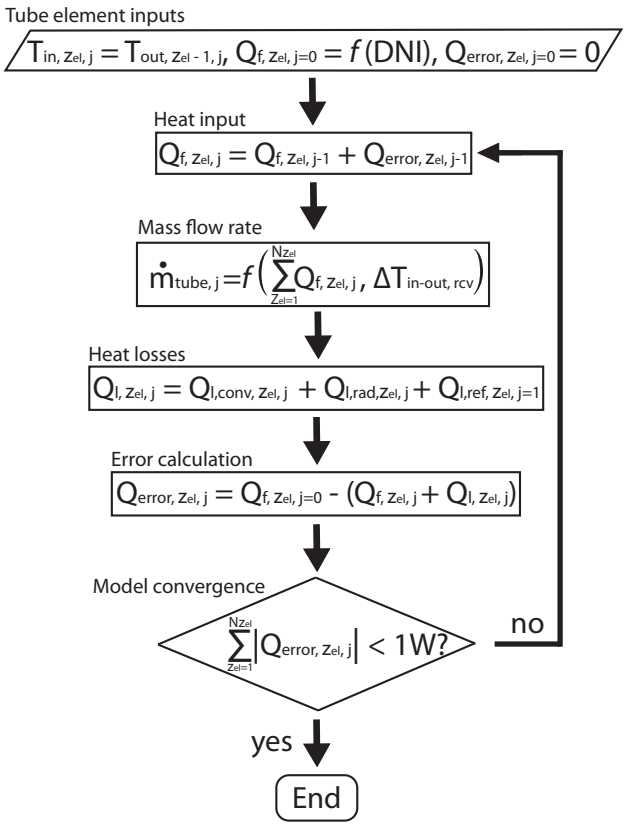


Figure 3: Flow diagram of iterative process used in the receiver thermal model to achieve an energy balance on tube axial elements ($z_{el}$)

The outlet temperature of one axial element forms the inlet temperature for the next element in the flow direction ($T_{in,z_{el}} = T_{out,z_{el}-1}$). The outlet temperature for each axial element is calculated as follows;

$$T_{out,z_{el}} = T_{in,z_{el}} + \frac{Q_{f,z_{el}}}{\dot{m}C_p} \tag{2}$$

The thermal energy absorbed by the fluid at various positions along the tube length ($Q_{f,z_{el}}$) is determined from the iteration procedure described in Figure 3. The fluid bulk temperature is the average of the inlet and outlet temperatures ($T_{f,z_{el}} = (T_{in,z_{el}} + T_{out,z_{el}})/2$), and is used to define the properties of the sodium HTF at each element $\left(\rho, k, \mu, C_p\right)$. For the first iteration step ($j = 1$), the total power falling on the receiver is assumed to be absorbed by the fluid, therefore the inner wall heat flux is equal to the outer wall heat flux $\left(\overset{"}{Q}_{si,z,\theta} = \overset{"}{Q}_{so,z,\theta}\right)$. For all other iteration steps ($j > 1$), the inner wall heat flux varies according to heat losses along the tube length and around the circumference.

Non-uniform thermal boundary conditions (Figure 2) negate the use of standard fluid-wall heat transfer calculation methods for a uniformly heated tube, and a different methodology must be employed. An analytical method developed by Gärtner et al. (1974) can be used to calculate the local Nusselt number ($Nu_{f,\theta}$) for a non-uniformly heated tube under turbulent flow conditions. The authors have developed a solution to the energy equation for a tube undergoing

non-axisymmetric heating conditions. Good agreement was found when the analytical method was compared to experimental data with air as the working fluid (data from Black and Sparrow (1967)), and while no such validation has been performed as yet for liquid metals ($Pr_f << 1$), this remains the best method known to the authors for non-uniform thermal boundary conditions. The method is applicable for any arbitrary circumferential heat flux distribution that can be represented by a Fourier series expression. The net heat flux distribution at an axial location on the tube is first averaged against $\pi$, $\bar{Q}^{"}_{si,z} = Q^{"}_{si,z}/\pi$, then the deviation of the local heat flux from the average is represented by a Fourier series expression, $Q^{"}_{si,z,\theta}/\bar{Q}^{"}_{si,z} = 1 + F_\theta$, where $F_\theta$ is found through the following;

$$F_\theta = \sum_{n=1}^{\infty} F_{n,\theta} = \sum_{n=1}^{\infty} a_n cos\,(n\theta) + b_n sin\,(n\theta) \tag{3}$$

The first iteration of the thermal model assumes that all heat falling on the receiver tube is transferred to the fluid $\left(Q^{"}_{si,z,j=1} = Q^{"}_{so,z}\right)$. Recognising that the heat flux distribution described by Equation 1 yields an even function, the $b_n$ coefficients go to zero forming a Fourier cosine series, and the $a_n$ coefficients for the initial heat flux profile are as follows (Pacheco et al., 1995);

$$a_1 = \frac{\pi}{2}, \quad a_n = \frac{sin\left(\frac{(1-n)\pi}{2}\right)}{1-n} + \frac{sin\left(\frac{(1+n)\pi}{2}\right)}{1+n} \tag{4}$$

Thermal losses from the tube are non-uniform due to the axial and circumferential temperature profiles, therefore the Fourier coefficients of following model iterations will vary slightly from those presented in Equation 4 for the inner wall heat flux $\left(Q^{"}_{si,z,j>1} \neq Q^{"}_{so,z}\right)$. Using the Fourier coefficients of the inner wall heat flux, the local Nusselt number around the tube circumference is found through the following;

$$Nu_{f,z,\theta} = \frac{2\left(Q^{"}_{si,z,\theta}/\bar{Q}^{"}_{si,z}\right)}{G_0 + \sum_{n=1}^{\infty} G_n F_{n,\theta}} = \frac{h_{f,z,\theta} D_i}{k} \tag{5}$$

Where $G_{0,n}$ are wall temperature functions at various harmonics found from solutions to the energy equation, tabulated by Gärtner et al. (1974) for a broad range of Reynolds ($10^4 \leq Re_f \leq 10^6$) and Prandtl number ($0 \leq Pr_f \leq 100$). With $Nu_{f,z,\theta}$ established, corresponding local heat transfer coefficients ($h_{f,z,\theta}$) are then used to calculate inner wall surface temperatures;

$$T_{si,z,\theta} = T_{f,z} + \frac{Q^{"}_{si,z,\theta}}{h_{f,z,\theta}} \tag{6}$$

The outer wall surface temperatures can then be established from the following equation by assuming one-dimensional conduction across the tube wall;

$$T_{so,z,\theta} = T_{si,z,\theta} + \frac{Q^{"}_{si,z,\theta}}{k_{tube}} \left(r_o \left(ln \frac{r_o}{r_i}\right)\right) \tag{7}$$

An assumption of radial-dominant conduction simplifies the analysis, however it is justified due to the significant

heat transfer coefficients associated with liquid sodium flows. The dominant heat transfer mechanism on the tube can be investigated with the Biot number ($Bi$). Convection dominant heat transfer can be assumed if the $Bi$ number is reasonably large ($Bi \geq 0.3$, Marugán-Cruz et al. (2016)), as is the case here.

Convective and radiative heat losses are evaluated from outer surface temperatures, while reflective losses are calculated from the incident energy on the receiver. Thermal losses through conduction in the backing insulation material comprise a very small percentage of the total heat loss from the tubes (Stoddard, 1986), and are therefore assumed negligible by treating the rear side of the receiver as adiabatic.

External convection occurs between the high temperature tube surface and the surrounding air according to Newtons law of cooling over the receiver unit. The average surface temperature across the receiver ($\bar{T}_{so,rcv}$) is used to calculate total heat lost through convection;

$$Q_{l,conv} = \bar{h} A_{rcv} \left( \bar{T}_{so,rcv} - T_{\infty} \right) \tag{8}$$

An ambient temperature ($T_{\infty}$) of $293K$ and an average wind speed of $5\,m/s$ are used in the analysis to calculate convective heat losses. The convective heat transfer coefficient ($\bar{h}$) is established from forced and natural convection $Nu$ correlations for flow over vertically aligned flat plates given by Siebers et al. (1983).

Thermal energy is lost from the receiver through re-radiation as high temperature tubes attempt to reach equilibrium with the ambient. The radiative view factor ($F_{view}$) between the tube and environment varies around the circumference due to its proximity with neighbouring tubes on the receiver, and is calculated using the crossed-strings method. The total radiative loss is found by calculating the losses for each circumferential element on the tube, and multiplying by the number of tubes on the receiver (making use of the assumption of a uniform heat flux where tube-to-tube conditions are assumed equal), thus accounting for local variations in temperature, emissivity, and view factor;

$$Q_{l,rad} = \sum_{tube=1}^{N_{tube}} \left( \sum_{z_{el}=1}^{N_{z_{el}}} \left( \sum_{\theta_{el}=1}^{N_{\theta_{el}}} \varepsilon \delta A_{\theta_{el}} F_{view} \left( T_{so}^4 - T_{\infty}^4 \right) \right) \right) \tag{9}$$

The Stefan-Boltzmann constant ($\delta$) is $5.67x10^{-8}\ W/m^2K^4$. Emissivity ($\varepsilon$) and absorptivity ($a_s$) are both very important characteristics of the receiver surface coating, directly influencing radiative and reflective losses respectively. A high temperature black paint is typically applied to receiver tubes in order to maximise solar absorptance and minimise thermal emittance. Using equations given by Ho et al. (2014) for Pyromark® 2500 paint, emissivity as a function of temperature is calculated (ranging between $\sim 0.8-0.9$), and the absorptivity as a function of the irradiance incidence angle is evaluated. A maximum absorptivity value of $a_s = 0.95$ occurs at the tube crown ($\theta = 0$), decreasing as the incidence angle varies from the normal. The reflective loss is found for each circumferential element on the tube, thus accounting for local variations in absorptivity, with the total reflective losses on the tube multiplied by the number of tubes on the receiver;

$$Q_{l,ref} = \sum_{tube=1}^{N_{tube}} \left( \sum_{z_{el}=1}^{N_{z_{el}}} \left( \sum_{\theta_{el}=1}^{N_{\theta_{el}}} Q_{so,\theta_{el}} \left(1 - a_s\left(\theta\right)\right) \right) \right) \tag{10}$$

Receiver thermal efficiency is found by subtracting thermal losses from the total energy concentrated on the receiver by the heliostat field ($Q_{net}$);

$$\eta_{th} = \frac{\left(Q_{net} - Q_{l,conv} - Q_{l,rad} - Q_{l,ref}\right)}{Q_{net}} \tag{11}$$

*2.2. Mechanical analysis*

The mechanical reliability of the receiver is estimated through a creep-fatigue analysis. Creep damage is accumulated in the tube material due to continuous plastic deformation caused by load controlled stresses occurring at high temperatures over time. Fatigue damage is built up over time when the receiver is thermally cycled due to cloud passages and diurnal events, which fluctuate tube temperatures and thus cause damaging thermal stress cycles. In order to assess the creep-fatigue damage of the receiver, tube stresses are initially established.

The receiver working fluid is shuttled from the cold storage tank to the receiver where its temperature is raised, and back to the hot storage tank. This action is performed using HTF pumps at a pressure that must overcome the pressure drop in the system and deliver the fluid at a desired flow rate. If a pressure differential exists between the inside and outside of the tube, stresses will be present in the wall;

$$\sigma_{r_{r,\theta,z}} = \frac{\left(P_i r_i^2 - P_o r_o^2\right)}{\left(r_o^2 - r_i^2\right)} + \frac{r_o^2 r_i^2 \left(P_o - P_i\right)}{r^2 \left(r_o^2 - r_i^2\right)} \tag{12}$$

$$\sigma_{\theta_{r,\theta,z}} = \frac{\left(P_i r_i^2 - P_o r_o^2\right)}{\left(r_o^2 - r_i^2\right)} - \frac{r_o^2 r_i^2 \left(P_o - P_i\right)}{r^2 \left(r_o^2 - r_i^2\right)} \tag{13}$$

$$\sigma_{z_{r,\theta,z}} = \frac{\left(P_i r_i^2 - P_o r_o^2\right)}{\left(r_o^2 - r_i^2\right)} \tag{14}$$

The internal fluid pressure ($P_i$) is assumed as $400\,kPa(G)$, this is the gauge pressure of the cold HTF pump at maximum load, while the external fluid pressure ($P_o$) is assumed as atmospheric. In reality, the fluid pressure will vary throughout operation as the mass flow rate is regulated to meet temperature demands for varying DNI levels, therefore an assumption of maximum fluid pressure throughout operation is conservative. The internal pressures seen here will result in small tube stresses in comparison to thermally induced loads, nevertheless they are an important consideration as they are a load controlled stress that are not self limiting.

When a tube is heated uniformly, it will expand freely, and no thermal stresses are present (Faupel and Fisher, 1981). However, when a non-uniform heating condition persists on a tube, the presence of a temperature differential

will result in differing thermal expansion conditions that cannot be freely accommodated in a continuous body, inducing thermal stresses. This is an important issue in receiver design as non-uniform temperatures exist on the tubes in the axial, radial and circumferential directions due to the heat transfer process.

It is commonplace to evaluate thermal stresses on non-isothermal tubes by accounting for radial temperature gradients only, and equations for this can be found in Faupel and Fisher (1981). This methodology is appropriate if the circumferential and axial temperature gradients are negligibly small in comparison to the radial temperature gradients (Rodríguez-Sánchez et al., 2014). In the present study, the axial temperature gradient is orders of magnitude smaller than the radial temperature gradient, and its contribution to thermal stresses on the tube is considered negligible due to the absence of severe hotspots or temperature 'spikes' (Irfan and Chapman, 2009). The circumferential temperature gradient is approximately the same order of magnitude as the radial temperature gradient however, therefore a methodology that accounts for non-uniform temperature profiles in both the radial and circumferential directions is employed.

Goodier (1957) presents a set of theoretical equations that are used to evaluate thermal stresses at an axial location ($z$) on the tube, where temperature varies around the circumference ($\theta$) and through the thickness ($r$). The following equations assume an isotropic homogeneous material that obey Hooke's law. The circumferential temperature profiles at the axial location are first represented by the coefficients of a Fourier expression, and become functions of $\theta$;

$$T_{si,\theta,z} = A_0 + A_1 cos\,\theta + B_1 sin\,\theta + ... \tag{15}$$

$$T_{so,\theta,z} = A'_0 + A'_1 cos\,\theta + B'_1 sin\,\theta + ... \tag{16}$$

Thermal stresses are calculated by superimposing the results of two parts due to contributions of both radial and circumferential temperature gradients. The first part involves calculating radial ($\sigma_r$) and hoop ($\sigma_\theta$) stresses for the radial temperature difference (cross-wall);

$$\sigma_{r_{r,\theta,z}} = \frac{E\alpha\left(A_0 - A'_0\right)}{2\left(1-\nu\right) log\left(\frac{r_o}{r_i}\right)}\left[-log\frac{r_o}{r} - \frac{r_i^2}{r_o^2 - r_i^2}\left(1 - \frac{r_o^2}{r^2}\right) log\left(\frac{r_o}{r_i}\right)\right] \tag{17}$$

$$\sigma_{\theta_{r,\theta,z}} = \frac{E\alpha\left(A_0 - A'_0\right)}{2\left(1-\nu\right) log\left(\frac{r_o}{r_i}\right)}\left[1 - log\frac{r_o}{r} - \frac{r_i^2}{r_o^2 - r_i^2}\left(1 + \frac{r_o^2}{r^2}\right) log\left(\frac{r_o}{r_i}\right)\right] \tag{18}$$

The second part accounts for the circumferential temperature difference (cross-tube);

$$\sigma_{r_{r,\theta,z}} = \kappa r\, cos\theta\left(1 - \frac{r_i^2}{r^2}\right)\left(\frac{r_o^2}{r^2} - 1\right) \tag{19}$$

$$\sigma_{\theta_{r,\theta,z}} = \kappa r\, cos\theta \left( \frac{r_i^2 r_o^2}{r^4} + \frac{r_i^2 + r_o^2}{r^2} - 3 \right) \tag{20}$$

$$\tau_{r\theta_{r,\theta,z}} = \kappa r\, sin\theta \left( 1 - \frac{r_i^2}{r^2} \right) \left( \frac{r_o^2}{r^2} - 1 \right) \tag{21}$$

The receiver utilises flexible hoses that permit tube thermal expansion in the axial direction that prevents buckling upon heating (Figure 1). Therefore, it is deemed appropriate to calculate the axial stress component ($\sigma_z$) using the following equation which assumes an annulment of axial forces and bending moments that would otherwise be brought about for a condition of zero axial displacement;

$$\sigma_{z_{r,\theta,z}} = -E\alpha \left( T - T_{avg} \right) + \left[ 2\kappa\nu \left( \frac{r_i^2 + r_o^2}{r^2} - 2 \right) + \kappa' \right] r\, cos\theta \tag{22}$$

Finally,

$$\kappa = -\frac{E\alpha}{2\left(1-\nu\right)} \left( \frac{A_1}{r_i} - \frac{A_1'}{r_o} \right) \frac{r_i^2 r_o^2}{r_o^4 - r_i^4} \tag{23}$$

$$\kappa' = E\alpha \left( \frac{A_1 r_i + A_1' r_o}{r_o^2 + r_i^2} \right) \tag{24}$$

The analysis assumes a constant optical efficiency for the heliostat field, therefore the incident DNI is used to characterise the various thermal states that can occur during receiver operation, allowing for the evaluation of mechanical damage for different creep loading conditions ($q$) and fatigue cycle types ($p$). DNI is assumed maximum at 1000 $W/m^2$ (~solar noon, clear sky, in a location with a good solar resource) and minimum at 0 $W/m^2$ (night time). When the DNI range is divided into steps of 50 $W/m^2$, there are 20 different creep loading conditions, and 210 unique fatigue cycles subject to investigation. The thermal analysis is used to calculate tube temperatures for the various DNI conditions, and the mechanical analysis is then used to calculate the thermal stresses and strains associated with each creep loading condition and thermal cycle type.

The ASME Boiler & Pressure Vessel Code: Section III - Subsection NH (ASME, 2007) is used to establish the creep-fatigue damage for the receiver designs using material and temperature dependent creep and fatigue data provided. The cumulative damage equation for this analysis is shown below;

$$Damage \leq \sum_{p=1}^{p=210} \left( \frac{n_d\left(DNI\right)}{N_d\left(\Delta\epsilon_{total}, T\right)} \right)_p + \sum_{q=1}^{q=20} \left( \frac{\Delta t_d\left(DNI\right)}{t_d\left(\sigma_{vM}, T\right)} \right)_q \tag{25}$$

The von Mises effective stress ($\sigma_{vM}$) in Equation 25 is established for load controlled stresses for creep damage, however it is also used in the results section to depict the effective stress state for individual contributions of thermal and pressure induced loading (Figure 14);

$$\sigma_{vM} = \sqrt{\frac{(\sigma_r - \sigma_\theta)^2 + (\sigma_\theta - \sigma_z)^2 + (\sigma_z - \sigma_r)^2 + 6\left(\tau_{r\theta}^2 + \tau_{\theta z}^2 + \tau_{zr}^2\right)}{2}} \tag{26}$$

The receiver is deemed capable of withstanding a lifetime of service if the creep-fatigue intersection falls inside the enveloped space shown in Figure 4. Material creep-fatigue damage envelopes are used to determine the reliability of the receiver when both creep and fatigue damage is occurring simultaneously, as is the case here due to a large total operating time, a large number of thermal cycles, high temperatures, and high stresses.

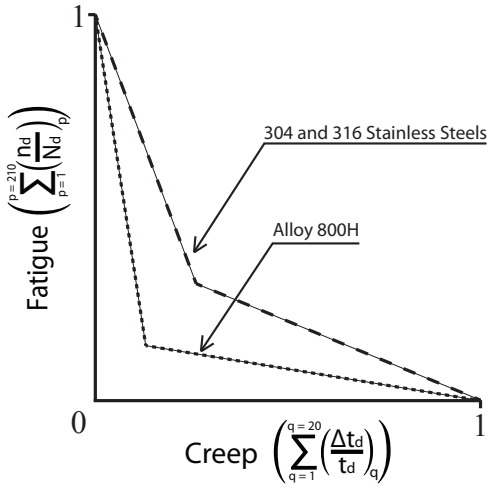


Figure 4: Creep-fatigue damage envelope used to assess mechanical reliability

The fatigue damage term is established for each cycle type using the total strain ($\Delta\epsilon_{total}$). The total strain is essentially the equivalent thermal strain modified by factors that account for local plasticity and creep, and is used to determine the number of allowable cycles ($N_d$) by entering it into material and temperature dependent design fatigue curves. The fatigue damage for each cycle is finally established by dividing the number of actual cycles ($n_d$) occurring over the receiver life by the allowable cycles, for each fatigue cycle type ($p$).

Creep damage is found by investigating the von Mises effective stress ($\sigma_{vM}$) (Fork et al., 2012) (Narayanan et al., 1984) of the load controlled stresses. This stress is used to determine the allowable stress to rupture time ($t_d$) based on the material temperature, and is divided by the total operational time ($\Delta t_d$) in order to determine the damage fraction for that creep load condition ($q$). The effect of stress relaxation is omitted in the evaluation of creep stress, as the stress is not expected to relax significantly between the relatively short thermal cycles that occur in solar receiver operation (Narayanan et al., 1984). The creep damage for each cycle is established by dividing the actual time spent at the elevated creep condition ($\Delta t_d$), into the allowable time ($t_d$). Load controlled stresses are assumed as the pressure induced membrane and bending stresses, and thermally induced membrane stresses (ASME, 2007). Thermally induced bending stresses are therefore assumed as a secondary stress. The steps used to conduct the mechanical analysis are shown in Figure 5.

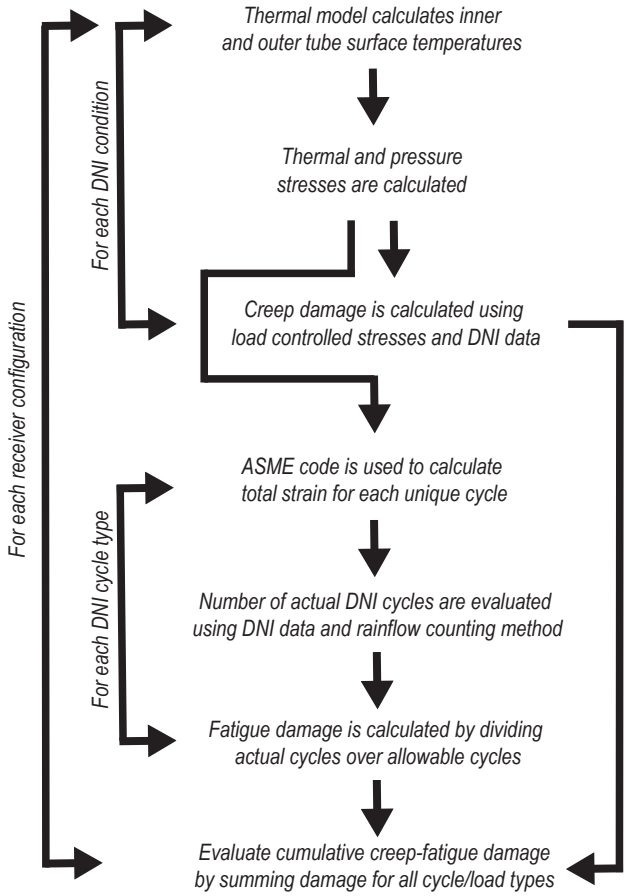


Figure 5: Flow diagram for mechanical analysis

The time periods spent at elevated temperatures for creep evaluation, and the actual cycle frequency for the calculation of fatigue is established by analysing DNI data from a weather station in Wagga Wagga, NSW, Australia (Bureau of Meteorology, 2015). The rain-flow counting technique is used to reduce a years worth of meteorological data into time spent at a particular DNI level, DNI cycle type, DNI cycle frequency, and has been extrapolated to 30 years in order to mimic the DNI conditions that a receiver may undergo during a life of operation.

### *2.3. Pressure drop analysis*

Consideration of the HTF pressure drop is important when comparing various receiver configurations. An increase in pressure drop will result in an increase in the necessary pumping power, meaning HTF pumps could potentially be a major parasitic load on the plant (Kolb et al., 2011), reducing the overall efficiency. A hydraulic analysis is therefore used to evaluate the HTF pressure drop in the receiver, and the associated pumping power requirement. The following equation is used to calculate the pressure drop through the receiver;

$$\Delta P_{rcv} = \sum_{z_{el}=1}^{N_{z_{el}}} f_{z_{el}} \left(\frac{L_{z_{el}}}{D_i}\right)\left(\frac{\rho U_{f,z_{el}}^2}{2}\right) \tag{27}$$

The friction factor is evaluated by using the Petukhov (1970) equation for fully developed turbulent flow in smooth tubes, which is applicable for the $Re$ across all designs investigated ($3000 \leq Re \leq 5x10^6$);

$$f_{z_{el}} = \frac{1}{\left(0.79ln\left(Re_{f,z_{el}}\right) - 1.64\right)^2} \tag{28}$$

The pressure drop across the receivers is then added to the pressure drop that exists across the remainder of the CSP plant ($\Delta P_{plant}$) for the calculation of required pumping power, using a conservative pump efficiency of $\eta_{pump} = 0.6$;

$$\dot{W}_{plant} = \frac{\dot{m}[(\Delta P_{rcv} \cdot N_{array}) + \Delta P_{plant}]}{\rho \eta_{pump}} \tag{29}$$

### *2.4. LCOE analysis*

The suitability of each configuration is investigated using the LCOE as the objective function, allowing for the identification of an appropriate receiver design for the representative plant. The LCOE valuation is typically used to measure the competitiveness of a power generation system, however it is used here as a tool to compare receiver configurations. Pertinent performance characteristics such as thermal efficiency, mechanical reliability, pumping parasitic load, and material costs are combined in order to determine an LCOE value for each design. The reference CSP plant is a modular 30 $MW_e$ plant with 89 solar arrays ($N_{array}$) supplying energy to a central power block (Vast Solar, 2017). Each solar array in the plant is made up of a tower and receiver unit, and a heliostat field with a total reflective area of $\sim 2500\,m^2$ ($A_{opt}$). For the purpose of comparing the various receiver configurations, the only variable considered here is the receiver, the cost of all other components are assumed fixed. The LCOE valuation of each receiver configuration has units of US $\$/kWh$, and is calculated using the following equation (Fraunhofer ISE, 2013);

$$LCOE = \frac{I_0 + \sum_{yr=1}^{N_{yr}} \frac{O\&M_{yr}}{(1+r_d)^{yr}}}{\sum_{yr=1}^{N_{yr}} \frac{Q_{yr,e}}{(1+r_d)^{yr}}} \tag{30}$$

LCOE is calculated for the full life of the plant from $yr = 1$ to the end of life at $N_{yr} = 30$. $I_0$ is the capital expenditure (CAPEX) of the full plant at $yr = 0$, and $O\&M_{yr}$ is the operation and maintenance costs of the plant in $yr = n$, both in units of US \$. $Q_{yr,e}$ is the electricity produced in $yr = n$, in units of $kWh$. $r_d$ is the plant discount rate applied throughout the plant lifetime, assumed here as 6% (Moore et al., 2014).

A conservative estimate for heliostat field CAPEX ($I_{0,opt}$) of 200 $\$/m^2$ and annual operation and maintenance costs of 65 $\$/kW_e - yr$ ($O\&M_{yr}$) are used in the analysis (Kolb, 2011). The heliostat fields are assumed accountable for 36% of the overall CAPEX (Pitz-Paal, 2005). A 5% share of the CAPEX is attributed to the billboard receivers, based on the least expensive design - a $1\,m^2$ receiver area made of 304 Stainless Steel tubing ($I_{0,rcv,base}$). Tube material costs

($I_{0,rcv,mat}$) depend on factors such as the supplier, tube geometry, and order quantity, therefore material prices from a number of different sources have been collated. The material cost difference between the three candidate materials is calculated by referring to 304 Stainless Steel ($I_{0,rcv,mat=304}$), the least expensive of the three, the next material is 316 Stainless Steel at $\sim$ 1.36 times the cost of 304 Stainless Steel, while Alloy 800H is the most expensive material at $\sim$ 5 times the cost of 304 Stainless Steel. Heat exchanger tubes are readily available and non-specialised engineering components, and are assumed to account for 10% of the base receiver CAPEX ($I_{0,rcv,tube}$), while the remainder is attributed to costs of insulation, support structures, headers, instrumentation, and heat trace equipment (Lovegrove and Stein, 2012). The costs associated with each receiver configuration ($I_{0,rcv}$) is dependent on the material type and the material quantity used, and the number of tube panel replacements ($N_{rep}$) required in 30 years due to creep deformation and fatigue damage.

$$I_0 = I_{0,opt}/0.36 \tag{31}$$

$$I_{0,opt} = (A_{opt} \cdot N_{array}) \cdot 200 \tag{32}$$

$$I_{0,rcv} = \left[\left(\left(I_{0,rcv,base} \cdot \left(1 - \frac{I_{0,rcv,tube}}{I_{0,rcv,base}}\right)\right) + \left(I_{0,rcv,base} \cdot \frac{I_{0,rcv,tube}}{I_{0,rcv,base}} \cdot \frac{I_{0,rcv,mat}}{I_{0,rcv,mat=304}}\right)\right) \cdot \left(\frac{A_{rcv}}{A_{rcv,base}}\right)\right] \cdot N_{rep} \tag{33}$$

$$I_{0,rcv,base} = I_0 \cdot 0.05 \tag{34}$$

The annual energy production is estimated by establishing the thermal energy ($Q_{yr,th}$) collected by the receivers using thermal efficiency values (Equation 11), an annual optical efficiency of 56.5% ($\eta_{opt}$) for an equator facing heliostat field (Ehrhart and Gill, 2014), and solar resource levels established from analysis of DNI data (Bureau of Meteorology, 2015). There is an assumed 5% thermal energy loss in system piping and thermal storage ($\eta_{trans}$), and a 33% Rankine cycle efficiency ($\eta_{pwr}$) (Pitz-Paal, 2005). The pressure drop penalty associated with each receiver configuration is incorporated into the LCOE study by subtracting the required pumping power from the output of the plant.

$$Q_{yr,e} = \left(Q_{yr,th} \cdot \eta_{trans} \cdot \eta_{pwr}\right) - \dot{W}_{yr} \tag{35}$$

$$Q_{yr,th} = \sum_{DNI=1}^{N_{DNI}} \left(DNI \cdot A_{opt} \cdot \eta_{opt} \cdot \eta_{th} \cdot N_{array} \cdot N_{hr}\right) \tag{36}$$

There are a number of simplifications made in the calculation of LCOE, however the analysis serves to identify the optimum receiver design rather than provide an accurate economic assessment of the representative CSP plant.

## 3. Results and discussion

There is little discrepancy between the three candidate materials in terms of thermal performance and pressure drop, therefore the results of the thermal and hydraulic analyses need only be presented here for one material.

The efficiency of the receiver is critical to the success of the plant. For a period of solar exposure, a larger receiver thermal efficiency will result in greater thermal energy available for steam production, meaning an increase in overall plant efficiency and reduced LCOE. The thermal efficiency of the receiver is largely dependent on the surface area used in the heat transfer process. Reflective losses are affected by the surface absorptivity, as per Equation 10, however convective and radiative losses are affected by the area used for heat transfer, as shown in Equations 8 & 9. A plot of thermal efficiency at maximum insolation conditions (design point, DNI = 1000 $W/m^2$) is shown in Figure 6 for a range of receiver areas and tube diameters.

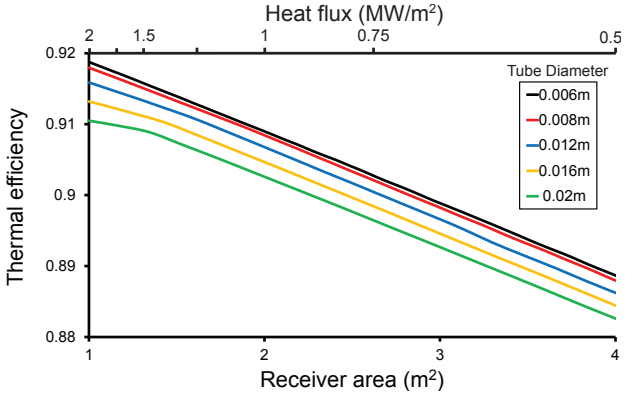


Figure 6: Thermal efficiency for receiver configurations of varying tube diameter and heat transfer area (304 Stainless Steel)

There is a marked gain in thermal performance between the smallest and largest heat transfer areas investigated. The increased thermal efficiency of smaller sized receivers will lower LCOE, due to the twofold effect of greater thermal energy yield for a period of solar exposure and reduced material costs. Thermal efficiency is influenced by the difference between surface temperatures and ambient, with a decreasing surface temperature resulting in greater thermal performance due to a reduction in radiative and convective losses. A smaller sized receiver results in an increase in surface temperature, as a greater heat flux exists across the surface. At maximum insolation conditions, the concentrated solar energy input from the field results in a heat flux variation from 2 $MW/m^2$ − 0.5 $MW/m^2$ across the designs investigated. The increase in surface temperature that comes about due to decreasing the area hinders the mechanism of reducing heat losses. However, results show that a reduction in heat transfer area is more influential than the resultant increase in surface temperatures on thermal efficiency. Figure 7 illustrates the various heat loss modes for varying receiver configurations with 0.012 $m$ diameter tubes.

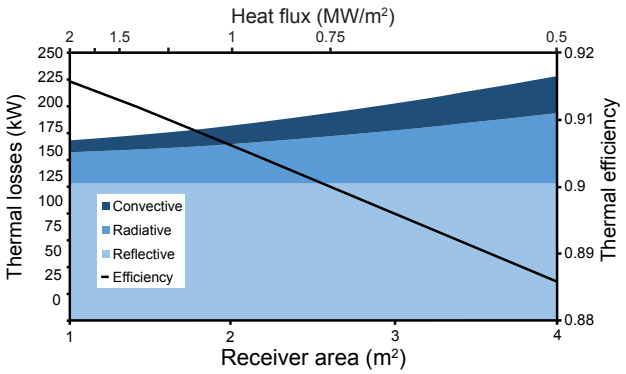


Figure 7: Thermal losses for various receiver configurations with $0.012\,m$ tube diameters (304 Stainless Steel)

Radiative and convective losses both increase with an increase in area, despite the consequential surface temperature decrease (Figure 8). Heat losses through reflection (Equation 10) contribute the greatest amount to the overall receiver losses, followed by radiation (Equation 9) and convection (Equation 8). A lower ambient temperature than that used in the analysis ($293\,K$) will result in greater losses through convection and radiation, while a higher ambient temperature will result in greater thermal performance as it reduces the temperature difference that drives convective and radiative loss modes. Convective losses will increase for a greater wind speed, as it triggers a larger heat transfer coefficient between the receiver and ambient. The $5\,m/s$ wind speed results in a mixed convection condition across all configurations using correlations provided by Siebers et al. (1983). The convection condition will transition to forced convection at more severe wind conditions resulting in greater losses, and purely free convection for lighter winds resulting in lower convective losses.

Of the designs investigated, the highest thermal efficiency is $\sim$ 91.9% for a $1\,m^2$ receiver area with $0.006\,m$ diameter tubing. The efficiency is influenced by tube parameters such as diameter, wall thickness, material thermal conductivity, absorptivity, emissivity, as well as surface temperatures and heat transfer area. In the present study, a standard wall thickness of $0.001\,m$ was maintained across all designs. Reducing wall thickness will result in lower cross wall temperature differences, resulting in greater thermal performance and helping to reduce thermal stresses. Tube wall thermal conductivity is similar for the three candidate materials investigated in this analysis, however it is important to use a highly conductive material in order to minimise the temperature difference across the wall, which lowers efficiency and drives thermomechanical damage. A high absorptivity can be achieved by applying a surface coating to the tubes that approximates a black-body, helping to minimise losses through reflection. A tube coating with a low emissivity value results in reduced losses through radiation. A number of selective coatings for solar receiver applications are under development, with the aim of maximising absorptivity and minimising thermal emittance (Ho et al., 2014).

Maximum tube temperatures occur at the outlet ($z/L_{tube} = 1$), towards the crown ($\theta = 0$), and are shown in Figure 8 for the various designs. Material data from ASME (2007) can be used to evaluate the mechanical reliability of

components up to temperatures of 978 $K$ for 304 and 316 Stainless Steel, and 1033 $K$ for Alloy 800H. Confidence in mechanical reliability predictions is greatly diminished if these temperature limits are breached, therefore, as indicated in Figure 8(a), configurations that surpass these temperature limits are excluded from selection. The inner wall temperatures can be used to indicate the maximum film temperature of the HTF. Sodium has a liquidus temperature range between 371 $K$ – 1156 $K$, therefore only receiver configurations with fluid temperatures within this range can be considered. As indicated in Figure 8(b), all receiver configurations investigated in this analysis fall within this liquidus temperature range, highlighting the high heat flux capabilities of sodium. Tube material temperatures are therefore more critical than the fluid film temperature for sodium receivers across the parameters investigated. The design of receivers utilising a less effective working fluid such as molten salt may be inhibited by the film temperature limit to a greater extent than sodium, this is due to lower tube heat transfer coefficients and a lower liquidus temperature range.

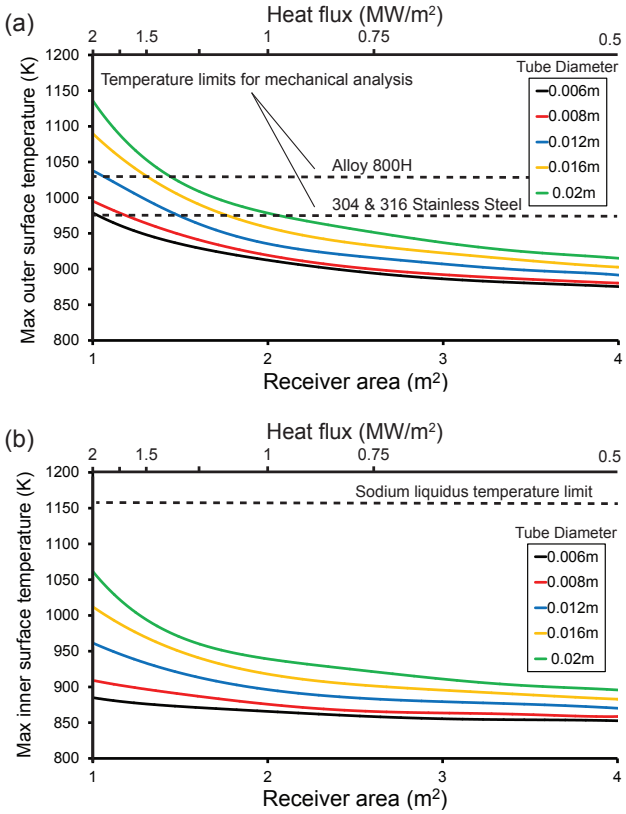


Figure 8: Maximum outer tube surface temperature ($T_{so,\theta}$), and inner tube surface temperatures ($T_{si,\theta}$), for receiver configurations of varying tube diameter and heat transfer area (304 Stainless Steel)

The large heat transfer coefficients associated with small diameter tubes means that the bulk sodium to wall temperature difference is smaller than that of larger diameters. Tube inner and outer wall temperatures therefore increase as the diameter increases, leading to greater thermal losses and reduced efficiency. A plot of the variation in local Nusselt number ($Nu_{f,\theta}$), and corresponding heat transfer coefficient ($h_{f,\theta}$) calculated from Equation 5 is shown

in Figure 9 for varying tube diameters at $z/L_{tube} = 1$ for $1\,m^2$ receiver areas. The $Nu_{f,\theta}$ varies significantly for the non-uniformly heated case to that of a uniformly heated case ($Nu_f = 6.3 + 0.0167Re_f^{0.85}Pr_{f,si}^{0.93}$, Sleicher and Rouse (1975)), especially near the crown. The non-uniformity of $Nu_{f,\theta}$ and $h_{f,\theta}$ is expected to be more pronounced for liquid metals ($Pr_f << 1$) than for more conventional fluids with a higher $Pr_f$ (Kays et al., 1980). The solution to the energy equation presented by Gärtner et al. (1974) for a turbulent flow in a non-uniformly heated tube recognised experimental evidence that circumferential eddy diffusivity near the wall is greater than radial eddy diffusivity due to a greater freedom of tangential motion. An increase in turbulent thermal energy transport by eddy conductivity (increasing with both $Pr_f$ and $Re_f$) effectively acts to lower the discrepancy of wall temperature variation that exists between a uniformly heated tube and a circumferentially non-uniformly heated tube, which is driven by $Nu_{f,\theta}$. As liquid metal heat transfer is dominated by molecular conductivity well into the turbulent flow regime, thermal energy transport via eddy conductivity is small. Therefore, a conventional fluid ($Pr_f > 0.7$) is expected to have a lower $Nu_{f,\theta}$ variation as eddy conductivity is transporting thermal energy around the tube wall, however the same phenomena is only expected to occur with liquid metals up to a very high $Re_f$ where the eddy transport of thermal energy becomes increasingly influential on the heat transfer mechanism.

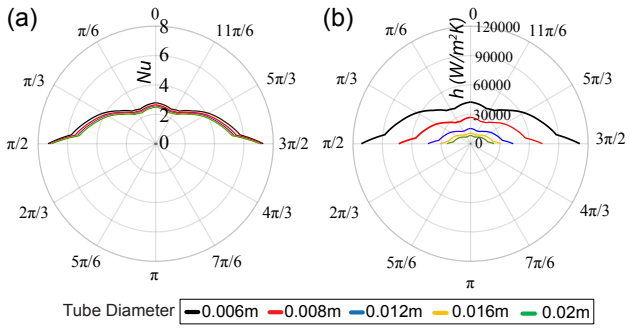


Figure 9: Polar plots of (a) local Nusselt number ($Nu_{f,\theta}$), and (b) corresponding local heat transfer coefficient ($h_{f,\theta}$) around the tube circumference for various tube diameters ($A_{rcv} = 1\,m^2$, $Q"_{so} \sim 2\,MW/m^2$, $z/L_{tube} = 1$, 304 Stainless Steel)

Tube inner wall temperatures ($T_{si,\theta}$) are calculated using the local heat transfer coefficient of the turbulent sodium flow and local heat flux ($Q"_{f,\theta}$) as per Equation 6, and it results in a non-uniform temperature profile around the circumference. There is a slight increase in $Nu_{f,\theta}$ for a decrease in tube diameter, this can be attributed to an increased $Re_f$, as seen in Figure 10 which depicts $Re_f$ averaged along the tube length. The lower level of heat loss associated with smaller tube diameters and receiver areas means that a greater portion of incident energy reaches the HTF ($Q_f$), and a greater HTF velocity is employed to achieve the desirable inlet-outlet $\Delta T$ ($573 - 843\,K$). That results in a greater $Re_f$ through receivers of small tube diameters and heat transfer areas. The mean fluid velocity over the tube length is shown in Figure 11.

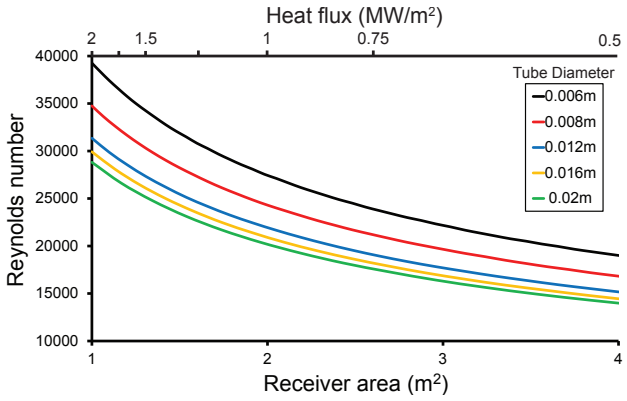


Figure 10: Mean HTF Reynolds number ($Re_f$) for receiver configurations of varying tube diameter and heat transfer area (304 Stainless Steel)

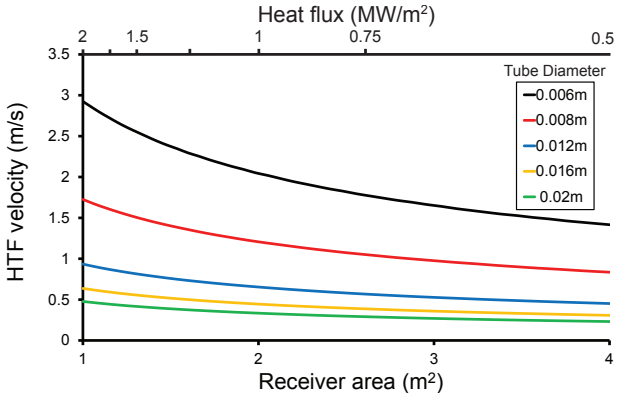


Figure 11: Mean HTF velocity through the receiver (304 Stainless Steel)

There is a $\sim$ 0.9% thermal efficiency gain to be achieved using $0.006\,m$ tubes over $0.02\,m$ across the range of receiver sizes investigated, while there is a a $\sim$ 3% gain between the maximum and minimum heat transfer areas. These gains can amount to a significant difference in thermal energy conversion over the life of the plant. A small tube diameter and receiver area should therefore be employed from a purely thermal performance standpoint.

The HTF pumping requirement plays a significant role in reducing the overall plant efficiency, therefore it is an important consideration in receiver design and HTF selection. Long piping loops shuttle the HTF from the cold storage tank to the receivers, and from the receiver back to the hot storage tank. These long sections induce a significant pressure drop, that can only be overcome by using highly powerful HTF pumps. In order to investigate the effect that the various receiver designs have on pumping requirements, the pressure drop across the radiated tube section of the receiver is calculated using Equations 27 - 28, and for completeness is summed with the pressure drop across a representative plant piping system. The pressure drop from the cold storage tank to the receiver is calculated as $357\,kPa$, and from the receiver through the heat exchanger and back to the cold tank is $254\,kPa$. The total pressure drop in the system for pump work calculations is therefore $611\,kPa$ plus the pressure drop across all receivers. The

pressure drop for the individual receiver, and the total pressure drop from the representative CSP plant is shown in Figure 12(a) for a range of configurations. To overcome the total pressure drop across the plant, HTF pumps need to be powered according to Equation 29. The total plant pumping power requirement is shown in Figure 12(b).

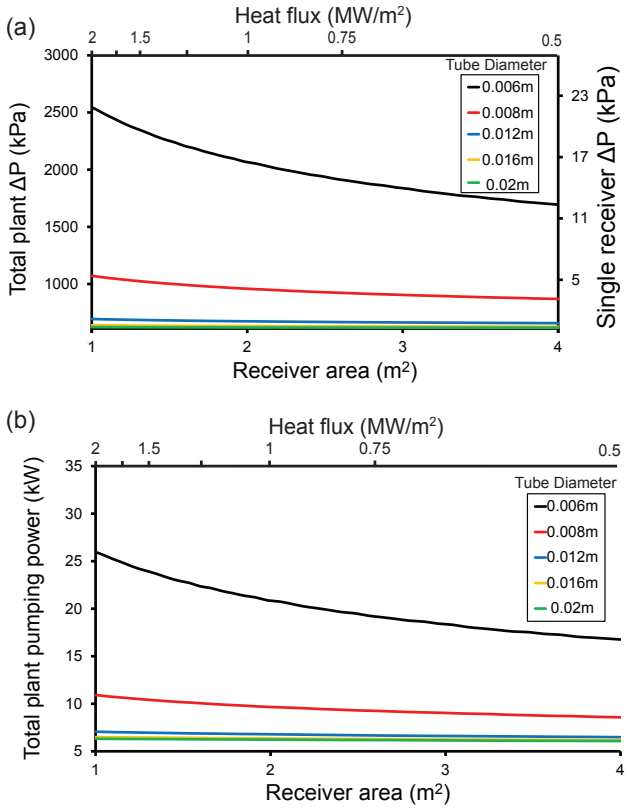


Figure 12: HTF Pressure drop ($\Delta P$) and pumping power requirement ($\dot{W}$) for receiver configurations of varying tube diameter and heat transfer area (304 Stainless Steel).

The pressure drop increases for a decrease in tube diameter, which results in a greater pumping power requirement due to a combination of flow passage decrease ($D_i$), and fluid velocity increase. A pumping power of $\sim 6.3\,kW$ is required to overcome the pressure drop throughout the plant, less the receivers, and this is therefore the minimum requirement. Larger tube diameters have a relatively small pressure drop penalty, and the majority of pumping power for these configurations is used to overcome pressure drop in various other piping sections of the plant. The $0.006\,m$ diameter experiences a significant pressure drop penalty, more than twice that of the $0.008\,m$ tube. As the thermal efficiency decreases with an increase in heat transfer area, the HTF mass flow rate must decrease in order to achieve the desired inlet-outlet $\Delta T$ (Equation 2). This results in a decrease in fluid velocity (Figure 11), and therefore a slightly reduced pressure drop penalty for larger receiver areas. From a purely hydraulic perspective, larger tube diameters and receiver areas should be employed in order to minimise the pressure drop penalty and necessary pumping power, however this inhibits thermal performance. An analysis of the net electrical power generated, such as the one con-

ducted in the present study for LCOE, allows for the selection of an optimum tube size as it takes into consideration both thermal performance and the pumping parasitic.

The creep and fatigue damage accumulated on the various receiver designs are shown in Figure 13. The corresponding reliability of the various designs in terms of survival years and necessary replacements is presented in Figure 15, which has been established based on the intersection point of the creep and fatigue terms on the damage envelope (Figure 4).

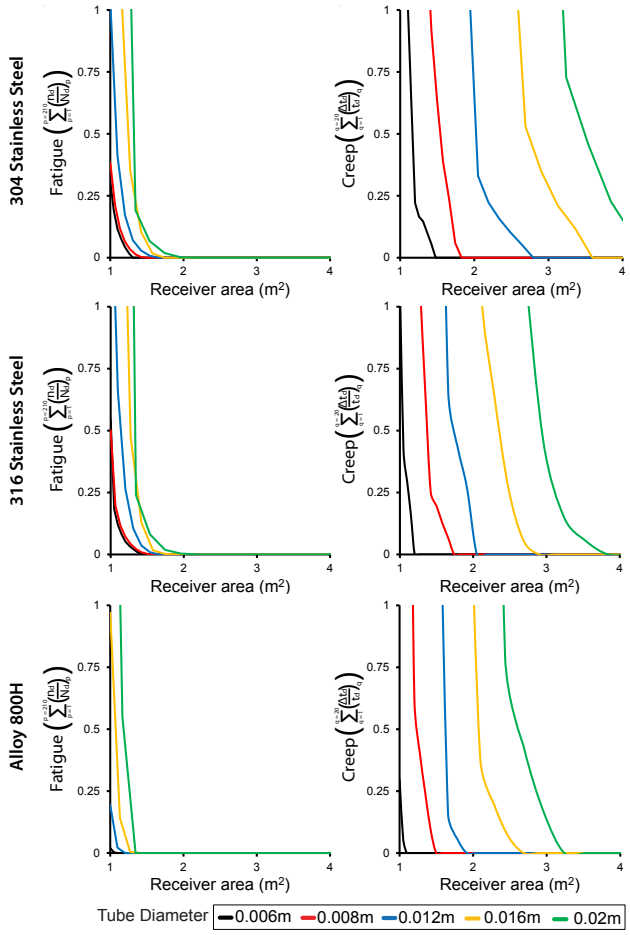


Figure 13: Fatigue and creep damage on receiver configurations for three different tube materials

Receiver failure is confirmed when the intersection of the cumulative creep and fatigue exceeds the boundaries of the damage envelope, as per Equation 25. The designs presented in Figure 13 that fall within the damage envelope have a mechanical reliability exceeding 30 years, and will not require replacement. This is indicated by Figure 15, where configurations that fall outside the envelope are seen to have a diminished mechanical life ($<$ 30 years), and will therefore require replacement(s).

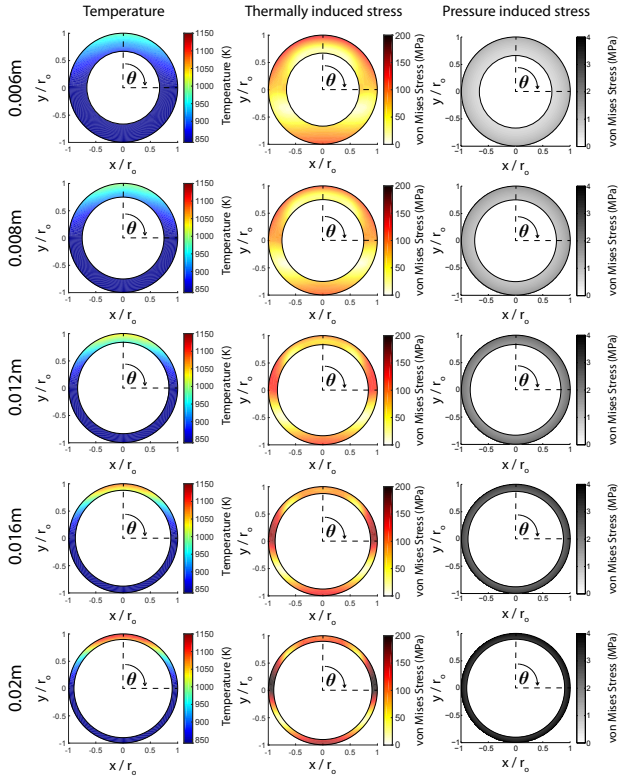


Figure 14: Plots of tube temperature, von Mises thermally induced stress, and von Mises pressure induced stress for various tube diameters at $z/L = 1$, all with a heat transfer area of $1\,m^2$

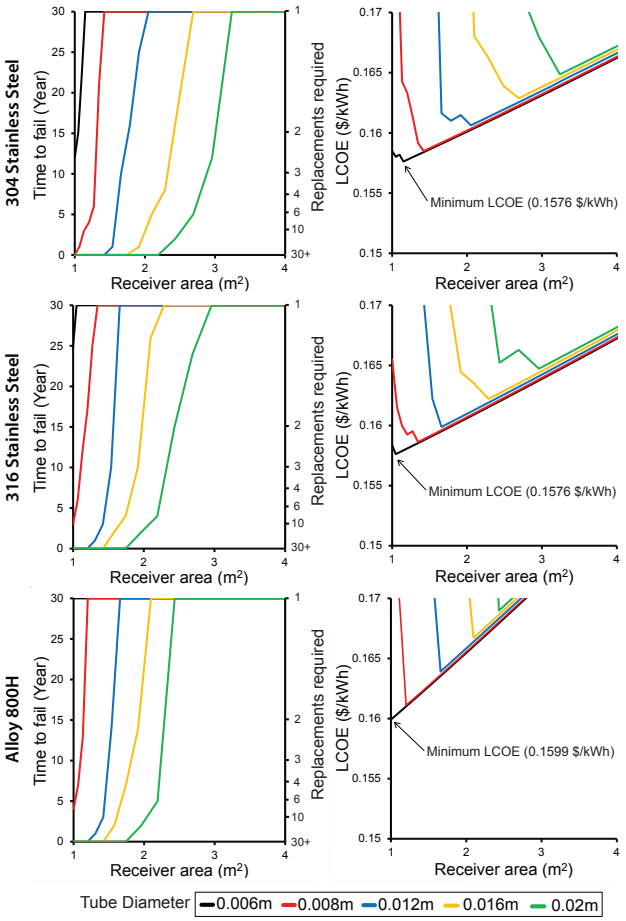


Figure 15: Time to failure and LCOE valuation of the various receiver configurations investigated for three different tube materials

Mechanical reliability increases with an increase in heat transfer area, and a decrease in tube diameter. As the internal fluid pressures are assumed constant across the various designs, there will be no variation on pressure induced stresses for receiver configurations that share the same tube diameter. The variation in mechanical life with changes in design are therefore influenced by thermally induced stresses. Higher incident heat flux levels associated with smaller sized receivers result in greater surface temperatures (Figure 8) and temperature gradients ($K/m$) across the tubes, resulting in increased thermal stresses. The resistance of the tube material to creep loads and fatigue cycles diminishes with an increase in both the driving stress and material temperature. Larger receiver designs are seen to have negligible creep and fatigue damage. In order to represent the effect that varying tube diameter has on tube stresses, plots of tube wall temperature and the corresponding von Mises effective stresses (total) for both thermal and pressure loads are presented in Figure 14;

Maximum material temperatures occur at the crown of the tube, where the incident heat flux is most intense, and decrease towards the bulk fluid temperature value where the tube is insulated (Equation 1). The radial temperature gradient is caused by the local heat flux which drives a temperature difference across the wall, and is influenced by

tube wall thickness and material thermal conductivity which increases with temperature. The radial gradient decreases at circumferential positions removed from the crown due to a decreasing local heat flux.

The circumferential temperature gradient is influenced by the difference between the maximum and minimum temperatures around the wall circumference, and the tube diameter. If we were to assume the same temperature profile for different tube diameters, the circumferential temperature gradient will increase for a decreasing tube diameter, increasing thermal stresses. As the tube diameters decrease in this study, thermal stresses generally decrease as tube temperatures decrease accordingly. However it is interesting to note that thermal stresses decrease as the tube diameter decreases towards the $0.008\,m$ tube, but increase again for the smallest tube diameter of $0.006\,m$. The lower material temperatures of the $0.006\,m$ tube negates this increase in thermal stress with respect to mechanical reliability, as the tube materials are more resistant to creep and fatigue damage at lower temperatures.

Pressure induced stresses increase as the tube diameter increases, with the maximum stress occurring at the inside wall, and decreasing slightly towards the outer surface. The internal fluid exerts an equal pressure in all directions, therefore the induced stress is uniform around the circumference. Although the magnitude of pressure induced stress is small, both the membrane and bending components are included as load controlled stresses in the calculation of creep damage.

Of the two failure mechanisms investigated, creep deformation is more restrictive on receiver design than fatigue damage. This can be viewed in Figure 13, where the fatigue damage fraction is zero for many receiver configurations where creep damage is a non-zero value. The large material temperatures that the receiver is expected to operate at over long periods of time results in a lower allowable time duration for a particular stress condition inflicting creep damage. Fatigue damage is a factor for very small receiver designs due to the large heat flux and large stress cycle magnitudes that occur during thermal cycles, however it tends towards a negligible value earlier than creep damage as the receiver area increases and maximum heat flux decreases.

The more costly Alloy 800H material is less susceptible to creep and fatigue damage than the stainless steel materials, and as such would be more suitable to high heat flux/temperature cycles that may be required in next generation receiver designs as CSP seeks to lower costs and maximize efficiency. From a mechanical reliability perspective, receivers using small tube diameters of Alloy 800H material operating under a small heat flux (large heat transfer area) will have minimum creep-fatigue damage and maximum reliability. However, it is apparent that a trade-off between contributing performance factors such as thermal efficiency, mechanical reliability, pumping requirement, and cost is required in order to select the optimum receiver design, and this can be made with an LCOE valuation (Equations 30-36, shown in Figure 15).

The lowest LCOE valuation for across the design space is shared for configurations that use both 304 Stainless Steel and 316 Stainless Steels, at $0.1576\,\$/kWh$. Both of these low cost designs use $0.006\,m$ tubes, with a mechanical reliability exceeding 30 years, however the mechanical superiority of 316 Stainless Steel means that a smaller heat transfer area (larger heat flux) design is possible. A smaller receiver design will reduce the structural requirements of the tower due to reduced dead-weight and wind loading, therefore the smaller 316 Stainless Steel design is deemed

superior. For receiver designs with a reliability exceeding 30 years, the 304 Stainless Steel designs generally have a lower LCOE valuation due to lower material costs. The thermal and hydraulic performance of all three materials is similar, therefore it is the associated material cost that separates them in the LCOE study as this influences capital costs in Equation 30. The LCOE study reveals that the enhanced thermal and mechanical performance of small diameter tubes cancels out the accompanying rise in pressure drop. LCOE increases significantly if receiver replacement is required, this is therefore a major factor for larger tube diameters on smaller sized designs.

The LCOE valuation is very much dependant on the assumptions made for cost and operation, however the same assumptions are made across all designs investigated therefore the optimum receiver design has been identified relative to the performance of all other designs. The LCOE value will vary for different receiver geometries, tube materials, HTF, variations in ambient wind speed and temperature, inlet-outlet temperature combinations, heat flux levels, and aiming strategies. This analysis serves the purpose of outlining the methodology that can be employed for analysing the pertinent performance characteristics that play a role in selecting the optimum receiver design for a CSP plant.

## 4. Conclusions

A thermal, mechanical, and hydraulic study has been presented for a liquid sodium billboard receiver with varying configurations of heat transfer area, tube diameter, and tube material. The main results of the analysis show that thermal performance increases for a decrease in heat transfer area, despite a resultant increase in surface temperature. Decreasing the tube diameter leads to increased heat transfer coefficients, leading to reduced surface temperatures and thermal losses. The large heat fluxes associated with small receiver areas incur large temperature gradients and surface temperatures, which increases thermal stresses and mechanical damage. A reduction in tube diameter will result in greater mechanical reliability as stresses and temperatures decrease. The mechanical reliability analysis shows that large heat fluxes can be accommodated using the liquid sodium HTF, as long as a small tube diameter is used to facilitate large heat transfer coefficients. The pressure drop penalty increases for a reduction in tube diameter, however the LCOE analysis shows that such a penalty may be tolerated for the benefit of thermal performance and mechanical reliability. The Alloy 800H designs are less susceptible to creep deformation and fatigue damage than both 304 and 316 Stainless Steel materials, however it does incur a significant cost penalty which nullifies its mechanical superiority from an LCOE standpoint. The analysis illustrates the importance of using a figure of merit such as LCOE in the design of solar receivers, as it factors relevant performance characteristics in order to deliver an optimum design based on a number of requirements.

## Acknowledgments

This research is funded by the Irish Research Council for Science, Engineering and Technology under the Enterprise Partnership Scheme in collaboration with Vast Solar.

## References


ASME, 2007. ASME Boiler & Pressure Vessel Code, Section III, Subsection NH, Class 1 Components in Elevated Temperature Service. The American Society of Mechanical Engineers, Fairfield, NJ.

Black, A., Sparrow, E. M., 1967. Experiments on turbulent heat transfer in a tube with circumferentially varying thermal boundary conditions. Journal of Heat Transfer 89 (3), 258–268.

Boerema, N., Morrison, G., Taylor, R., Rosengarten, G., 2012. Liquid sodium versus Hitec as a heat transfer fluid in solar thermal central receiver systems. Solar Energy 86 (9), 2293–2305.

Bureau of Meteorology, 2015. One minute solar data. http://www.bom.gov.au/climate/data/oneminsolar/about-IDCJAC0022.shtml[accessed: 16 June 2015].

Coventry, J., Andraka, C., Pye, J., Blanco, M., Fisher, J., 2015. A review of sodium receiver technologies for central receiver solar power plants. Solar Energy 122, 749–762.

Ehrhart, B., Gill, D., 2014. Evaluation of annual efficiencies of high temperature central receiver concentrated solar power plants with thermal energy storage. Energy Procedia 49, 752–761.

Falcone, P. K., 1986. A handbook for solar central receiver design. Tech. rep., Sandia National Labs., Livermore, CA (USA).

Faupel, J. H., Fisher, F. E., 1981. Engineering design: a synthesis of stress analysis and materials engineering. Wiley.

Fink, J., Leibowitz, L., 1995. Thermodynamic and transport properties of sodium liquid and vapor. Tech. rep., Argonne National Lab., IL (United States).

Fork, D. K., Fitch, J., Ziaei, S., Jetter, R. I., 2012. Life estimation of pressurized-air solar-thermal receiver tubes. Journal of Solar Energy Engineering 134 (4), 041016.

Fraunhofer ISE, 2013. Levelized cost of electricity renewable energy technologies. https://www.ise.fraunhofer.de/content/dam/ise/en/documents/publications/studies/Fraunhofer-ISE_LCOE_Renewable_Energy_technologies.pdf[accessed: 20 June 2017].

Gärtner, D., Johannsen, K., Ramm, H., 1974. Turbulent heat transfer in a circular tube with circumferentially varying thermal boundary conditions. International Journal of Heat and Mass Transfer 17 (9), 1003–1018.

Goodier, J., 1957. Thermal stress and deformation. Journal of Applied Mechanics 24 (3), 467–471.

Ho, C. K., Iverson, B. D., 2014. Review of high-temperature central receiver designs for concentrating solar power. Renewable and Sustainable Energy Reviews 29, 835–846.

Ho, C. K., Mahoney, A. R., Ambrosini, A., Bencomo, M., Hall, A., Lambert, T. N., 2014. Characterization of pyromark 2500 paint for high-temperature solar receivers. Journal of Solar Energy Engineering 136 (1), 014502.

IEA, 2014. Technology Roadmap: Solar Thermal Electricity. International Energy Agency.

IEA, 2015. Trends 2015 in Photovoltaic Applications. International Energy Agency.

IRENA, 2012. Renewable Energy Cost Analysis: Concentrated Solar Power. International Renewable Energy Agency.

Irfan, M. A., Chapman, W., 2009. Thermal stresses in radiant tubes due to axial, circumferential and radial temperature distributions. Applied Thermal Engineering 29 (10), 1913–1920.

Kays, W., Crawford, M., Weigand, B., 1980. Convective heat transfer.

Kolb, G. J., 2011. An evaluation of possible next-generation high-temperature molten-salt power towers. Sandia National Laboratories, Albuquerque, NM, Report No. SAND2011-9320.

Kolb, G. J., Ho, C. K., Mancini, T. R., Gary, J. A., 2011. Power tower technology roadmap and cost reduction plan. SAND2011-2419, Sandia National Laboratories, Albuquerque, NM 7.

Lata, J. M., Rodríguez, M., de Lara, M. Á., 2008. High flux central receivers of molten salts for the new generation of commercial stand-alone solar power plants. Journal of Solar Energy Engineering 130 (2), 021002.

Liao, Z., Li, X., Xu, C., Chang, C., Wang, Z., 2014. Allowable flux density on a solar central receiver. Renewable Energy 62, 747–753.

Lovegrove, K., Stein, W., 2012. Concentrating solar power technology: principles, developments and applications. Elsevier.

Marugán-Cruz, C., Flores, O., Santana, D., García-Villalba, M., 2016. Heat transfer and thermal stresses in a circular tube with a non-uniform heat flux. International Journal of Heat and Mass Transfer 96, 256–266.

Moore, J., Grimes, R., Walsh, E., O'Donovan, A., 2014. Modelling the thermodynamic performance of a concentrated solar power plant with a novel modular air-cooled condenser. Energy 69, 378–391.

Narayanan, T., Carli, G., Rao, M., 1984. Structural design and life assessment of a molten salt solar receiver. Am. Soc. Mech. Eng.,(Pap.);(United States) 84 (CONF-840647-).

Pacheco, J. E., Ralph, M. E., Chavez, J. M., Dunkin, S. R., Rush, E. E., Ghanbari, C. M., Matthews, M., 1995. Results of molten salt panel and component experiments for solar central receivers: cold fill, freeze/thaw, thermal cycling and shock, and instrumentation tests. Tech. rep., Sandia National Labs., Albuquerque, NM (United States).

Pacio, J., Fritsch, A., Singer, C., Uhlig, R., 2014. Liquid metals as efficient coolants for high-intensity point-focus receivers: implications to the design and performance of next- generation CSP systems. Energy Procedia 49, 647–655.

Pacio, J., Wetzel, T., 2013. Assessment of liquid metal technology status and research paths for their use as efficient heat transfer fluids in solar central receiver systems. Solar Energy 93, 11–22.

Petukhov, B., 1970. Heat transfer and friction in turbulent pipe flow with variable physical properties. Advances in heat transfer 6 (503), i565.

Pitz-Paal, R., 2005. ECOSTAR: European Concentrated Solar Thermal Road-Mapping; Roadmap Document (WP 3 Deliverable No. 7). DLR.

Rodríguez-Sánchez, M. R., Soria-Verdugo, A., Almendros-Ibáñez, J. A., Acosta-Iborra, A., Santana, D., 2014. Thermal design guidelines of solar power towers. Applied Thermal Engineering 63 (1), 428–438.

Salomé, A., Chhel, F., Flamant, G., Ferrière, A., Thiery, F., 2013. Control of the flux distribution on a solar tower receiver using an optimized aiming point strategy: Application to themis solar tower. Solar Energy 94, 352–366.

Schiel, W. J., Geyer, M. A., 1988. Testing an external sodium receiver up to heat fluxes of 2.5 MW/m$^2$: Results and conclusions from the IEA-SSPS high flux experiment conducted at the central receiver system of the Plataforma Solar de Almeria (Spain). Solar energy 41 (3), 255–265.

Siebers, D. L., Schwind, R. G., Moffatt, R., 1983. Experimental mixed convection heat transfer from a large, vertical surface in a horizontal flow. Ph.D. thesis, Stanford University.

Sleicher, C., Rouse, M., 1975. A convenient correlation for heat transfer to constant and variable property fluids in turbulent pipe flow. International Journal of Heat and Mass Transfer 18 (5), 677–683.

Slocum, A. H., Codd, D. S., Buongiorno, J., Forsberg, C., McKrell, T., Nave, J.-C., Papanicolas, C. N., Ghobeity, A., Noone, C. J., Passerini, S., et al., 2011. Concentrated solar power on demand. Solar Energy 85 (7), 1519–1529.

Stoddard, M., 1986. Convective loss measurements at the 10 MWe solar thermal central receiver pilot plant. Sandia National Laboratories report SAND85-8250.

Vast Solar, 2017. In correspondence with site/design engineers, http://www.vastsolar.com/.